Supplemental Material
Room temperature magnetic vortices in the 2D magnet Fe_5GeTe_2

Elias Sfeir,[1] Carolin Schrader,[1] Florentin Fabre,[1] Jules Courtin,[2]
Céline Vergnaud,[2] Alain Marty,[2] Matthieu Jamet,[2] Frédéric Bonell,[2]
Isabelle Robert-Philip,[1] Vincent Jacques,[1] and Aurore Finco[1,*]

[1] *Laboratoire Charles Coulomb, Université de Montpellier, CNRS, Montpellier, France*
[2] *Université Grenoble Alpes, CNRS, CEA, SPINTEC, 38054 Grenoble, France.*

CONTENTS

* aurore.finco@umontpellier.fr

I. MACROSCOPIC CHARACTERIZATION OF THE SAMPLE

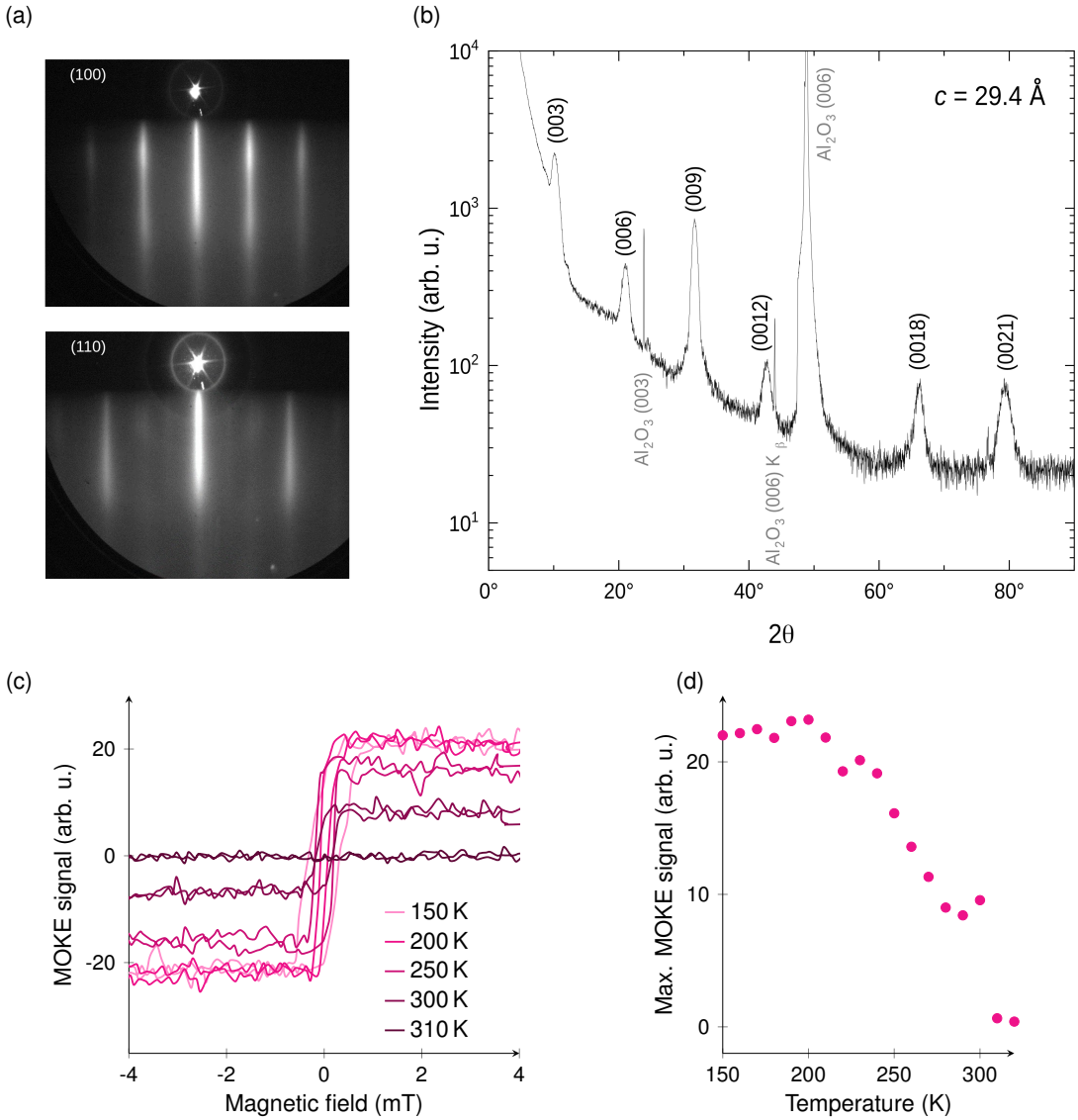

FIG. S1. (a) RHEED patterns, measured on the Fe_5GeTe_2 film before microstructuring, in the (100) and (110) reciprocal directions. (b) Out-of-plane $\theta/2\theta$ X-ray diffraction scan (Co source $K\alpha = 1.79$ Å). The measured c lattice parameter is 29.4 Å (= 3 layers) (c) MOKE hysteresis loops measured on the sample before patterning, and showing that it remains ferromagnetic up to 300 K. (d) Maximal MOKE signal recorded as a function of temperature, before patterning too. This signal is proportional to M_s.

II. CALIBRATION OF THE DIAMOND PROBE

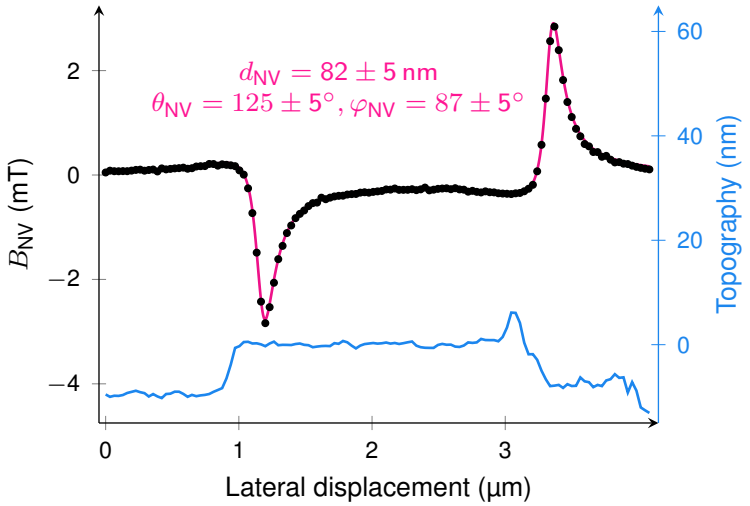

FIG. S2. Calibration experiment of the diamond probe. The measurement is performed on a 2 µm-wide ferromagnetic stripe, with the following composition: $TaN_{0.7\%}$ (1 nm)|$Co_{20}Fe_{60}B_{20}$ (1 nm)|MgO (2 nm) and analyzed following the method detailed in ref. [1]. The indicated value of d_{NV} takes into account the 3 nm-thick Al capping layer.

III. STRAY FIELD FROM THE EDGE OF A UNIFORMLY MAGNETIZED FILM

We derive here the analytic formula of the stray field present at the edge of an in-plane magnetized layer, which we used to extract the value of M_s in Fig. 2. We consider a semi-infinite film with an edge parallel to the y direction, located at $x = x_0$ and the orientation of the magnetization $\vec{M}$ is decribed by the angles θ_M and φ_M, as depicted on the sketch below.

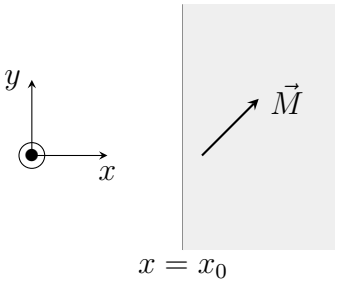

$$\vec{M} = M \begin{pmatrix} \cos\varphi_M \sin\theta_M \\ \sin\varphi_M \sin\theta_M \\ \cos\theta_M \end{pmatrix}$$

We can write the stray field $\vec{B}(\vec{r})$ as

$$\vec{B}(\vec{r}) = \frac{\mu_0}{4\pi} \int_{z'=-\frac{t}{2}}^{\frac{t}{2}} \int_{x'=x_0}^{+\infty} \int_{y'=-\infty}^{+\infty} \left(\frac{3(\vec{r}-\vec{r'})(\vec{M}\cdot(\vec{r}-\vec{r'}))}{|\vec{r}-\vec{r'}|^5} - \frac{\vec{M}}{|\vec{r}-\vec{r'}|^3} \right) \mathrm{d}x'\,\mathrm{d}y'\,\mathrm{d}z' \quad (1)$$

We compute each spatial component separately. Note that as the problem is invariant under a translation along the y axis, $B_y(\vec{r}) = 0$. We start with B_x:

$$B_x(\vec{r}) = \frac{\mu_0 M}{4\pi} \int_{z'=-\frac{t}{2}}^{\frac{t}{2}} \int_{x'=x_0}^{+\infty} \int_{y'=-\infty}^{+\infty} \left[\frac{3(x-x')\left[(x-x')\cos\varphi_M \sin\theta_M + (y-y')\sin\varphi_M \sin\theta_M + (z-z')\cos\theta_M\right]}{\left[(x-x')^2+(y-y')^2+(z-z')^2\right]^{\frac{5}{2}}} - \frac{\cos\varphi_M \sin\theta_M}{\left[(x-x')^2+(y-y')^2+(z-z')^2\right]^{\frac{3}{2}}} \right] \mathrm{d}x'\,\mathrm{d}y'\,\mathrm{d}z'$$

Everything can be integrated analytically, leading to:

$$\boxed{\begin{aligned} B_x(\vec{r}) = &-\frac{\mu_0 M}{2\pi} \left[\cos\varphi_M \sin\theta_M \left(\arctan\left(\frac{z+\frac{t}{2}}{x-x_0}\right) - \arctan\left(\frac{z-\frac{t}{2}}{x-x_0}\right)\right) \right. \\ &\left. + \frac{\cos\theta_M}{2} \left(\log\left(\left(z+\frac{t}{2}\right)^2 + (x-x_0)^2 \right) - \log\left(\left(z-\frac{t}{2}\right)^2 + (x-x_0)^2 \right)\right)\right] \end{aligned}} \quad (2)$$

A similar calculation for the component $B_z(\vec{r})$ results in:

$$\boxed{\begin{aligned} B_z(\vec{r}) = &\frac{\mu_0 M}{2\pi} \left[\cos\theta_M \left(\arctan\left(\frac{z+\frac{t}{2}}{x-x_0}\right) - \arctan\left(\frac{z-\frac{t}{2}}{x-x_0}\right)\right) \right. \\ &\left. - \frac{\cos\varphi_M \sin\theta_M}{2} \left(\log\left((z+\frac{t}{2})^2 + (x-x_0)^2 \right) - \log\left((z-\frac{t}{2})^2 + (x-x_0)^2 \right)\right)\right] \end{aligned}} \quad (3)$$

An interesting case is the limit $t \ll z$, meaning that the thickness of the film is much smaller than the distance between the NV center and the sample. Assuming this, we can simplify Eqs 2 and 3 and write:

$$\begin{cases} B_x(\vec{r}) = -\dfrac{\mu_0 M t}{2\pi} \dfrac{\cos\varphi_M \sin\theta_M (x - x_0) + \cos\theta_M z}{z^2 + (x - x_0)^2} \\ B_y(\vec{r}) = 0 \\ B_z(\vec{r}) = \dfrac{\mu_0 M t}{2\pi} \dfrac{\cos\theta_M (x - x_0) - \cos\varphi_M \sin\theta_M z}{z^2 + (x - x_0)^2} \end{cases} \tag{4}$$

IV. ESTIMATION OF THE ERROR IN THE EXTRACTION OF M_s

We detail here the procedure used to estimate the uncertainty ε on the estimation of M_s, which was previously applied in refs. [2, 3]. The total uncertainty is obtained from the fitting procedure itself and from the uncertainties on the parameters involved. Here these parameters are d_{NV}, t, θ_{NV}, φ_{NV}, θ_{M} and φ_{M}. Writing all these parameters as p_i, we express them as $p_i = \bar{p_i} \pm \sigma_{p_i}$ with $\bar{p_i}$ their nominal value and σ_{p_i} their uncertainty. The parameters describing the position and orientation of the NV center are obtained from the independent measurement shown in Fig. S2, the thickness is known from the growth procedure and the orientation of the magnetization is inferred from the images, and thus assumed to be parallel to the y axis. The extracted M_s value is obtained from a fit with the parameters set to their nominal values $\bar{p_i}$.

The uncertainty ε_{p_i} introduced by each parameter p_i is calculated by performing the fit with $p_i = \bar{p_i} + \sigma_{p_i}$ and $p_i = \bar{p_i} - \sigma_{p_i}$ while all the other parameters p_j are kept at their nominal value $\bar{p_j}$. The resulting values of M_s are denoted as $M_s(\bar{p_i} + \sigma_{p_i})$ and $M_s(\bar{p_i} - \sigma_{p_i})$. Then we compute ε_{p_i}:

$$\varepsilon_{p_i} = \frac{|M_s(\bar{p_i} + \sigma_{p_i}) - M_s| + |M_s(\bar{p_i} - \sigma_{p_i}) - M_s|}{2M_s} \tag{5}$$

Finally, we get the total uncertainty from:

$$\varepsilon = \sqrt{\varepsilon_{\mathrm{fit}}^2 + \sum_i \varepsilon_{p_i}^2} \tag{6}$$

since we assume that all the errors are independent. Tables below gather the data for the 4 calculations of M_s shown in Fig. 2. The average value of M_s is $202 \pm 12\,\mathrm{kA\,m^{-1}}$, where we used the standard deviation of the 4 measurements as the uncertainty.

Parameter	**Value**	**Uncertainty**	**Resulting error (%)**
d_{NV}	119 nm	± 20 nm	9%
t	11.8 nm	± 0.3 nm	2.5%
θ_{NV}	125°	± 5°	0%
φ_{NV}	87°	± 5°	0.4%
θ_{M}	90°	± 5°	0%
φ_{M}	90°	± 10°	1.7%
Fit error		$5.5\,\mathrm{kA\,m^{-1}}$	3%
			Total error: 10%

TABLE I. Uncertainty estimation for the fit presented in Fig. 2(a), yielding $M_s = 200 \pm 20\,\mathrm{kA\,m^{-1}}$.

Parameter	Value	Uncertainty	Resulting error (%)
d_{NV}	96 nm	± 20 nm	11%
t	11.8 nm	± 0.3 nm	2.5%
θ_{NV}	125°	± 5°	0.2%
φ_{NV}	87°	± 5°	0.4%
θ_{M}	90°	± 5°	0.3%
φ_{M}	90°	± 10°	0.5%
Fit error		7.5 kA m^{-1}	4.7%
			Total error: 12.2%

TABLE II. Uncertainty estimation for the fit presented in Fig. 2(b), yielding $M_s = 168 \pm 20\,\mathrm{kA\,m^{-1}}$.

Parameter	Value	Uncertainty	Resulting error (%)
d_{NV}	127 nm	± 20 nm	8.2%
t	11.8 nm	± 0.3 nm	2.5%
θ_{NV}	125°	± 5°	0%
φ_{NV}	87°	± 5°	0.3%
θ_{M}	90°	± 5°	0%
φ_{M}	90°	± 10°	0.4%
Fit error		8.3 kA m^{-1}	4.3%
			Total error: 9.6%

TABLE III. Uncertainty estimation for the fit presented in Fig. 2(c), yielding $M_s = 205 \pm 20\,\mathrm{kA\,m^{-1}}$.

Parameter	Value	Uncertainty	Resulting error (%)
d_{NV}	137 nm	± 20 nm	7.1%
t	11.8 nm	± 0.3 nm	2.5%
θ_{NV}	125°	± 5°	0%
φ_{NV}	87°	± 5°	0.4%
θ_{M}	90°	± 5°	0.1%
φ_{M}	90°	± 10°	0.5%
Fit error		7.1 kA m^{-1}	3.2%
			Total error: 8.2%

TABLE IV. Uncertainty estimation for the fit presented in Fig. 2(d), yielding $M_s = 234 \pm 19\,\mathrm{kA\,m^{-1}}$.

V. EVOLUTION OF M_s WITH THE AREA OF THE MICROSTRUCTURE

Although the effect remains rather small and cannot be compared with the spectacular increase in T_C measured on Fe_3GeTe_2 when patterning it using Ga ions [4], Fig. S3 could indicate a correlation between M_s and the area of the microstructure. The trend is opposite to the effect of Ga, as patterning smaller structures seems to lead to a smaller M_s. In our case, the effect could be the consequence of damages made to the film during the patterning procedure.

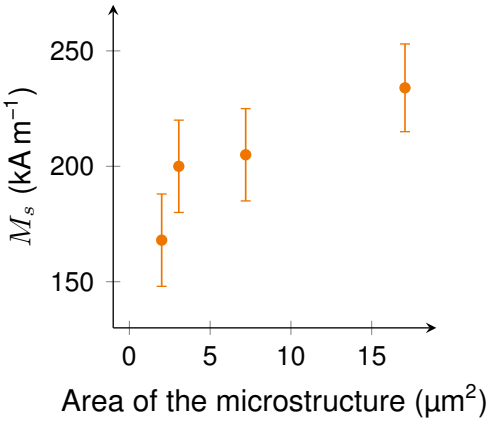

FIG. S3. Dependence of M_s on the area of the investigated rectangle, the data is extracted from Fig. 2. We observe a small increase of M_s with the area.

VI. CHOICE OF K_u IN THE MICROMAGNETIC SIMULATIONS OF THE VORTICES

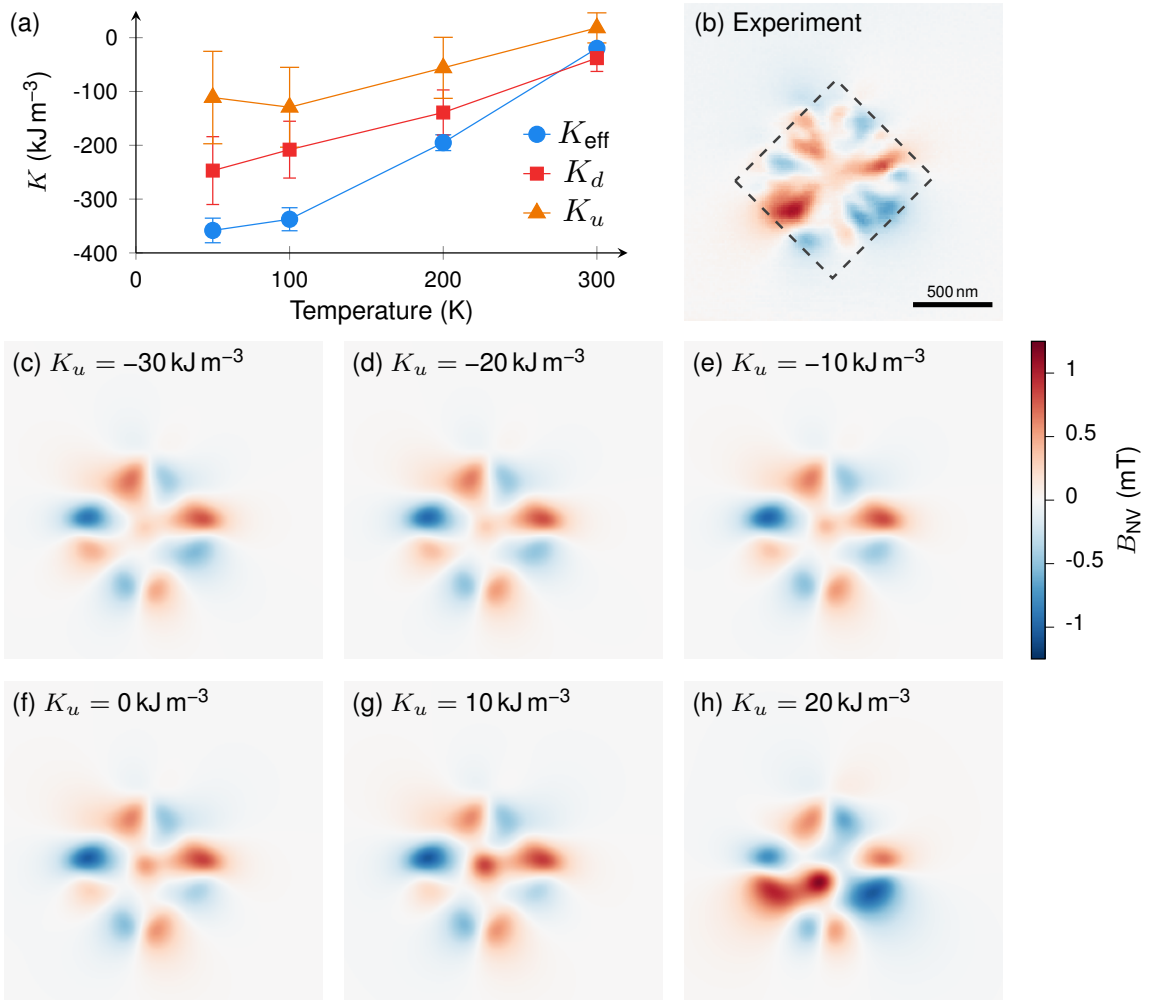

FIG. S4. (a) SQUID measurement of the effective anisotropy K_{eff}, which, combined with the measurement of M_s in Fig. 1 providing the shape anisotropy K_d, allows us to obtain the value of the uniaxial anisotropy K_u. K_u is very small at room temperature. (b) Measured magnetic stray field map of a vortex in a $1 \times 1\,\mu\text{m}^2$ Fe_5GeTe_2 square. (c)-(h) Magnetic stray field maps from vortex configurations obtained with micromagnetic simulations, with the same parameters as specified in the main text except K_u, which is varied in the different panels.

VII. VORTICES IN DISKS

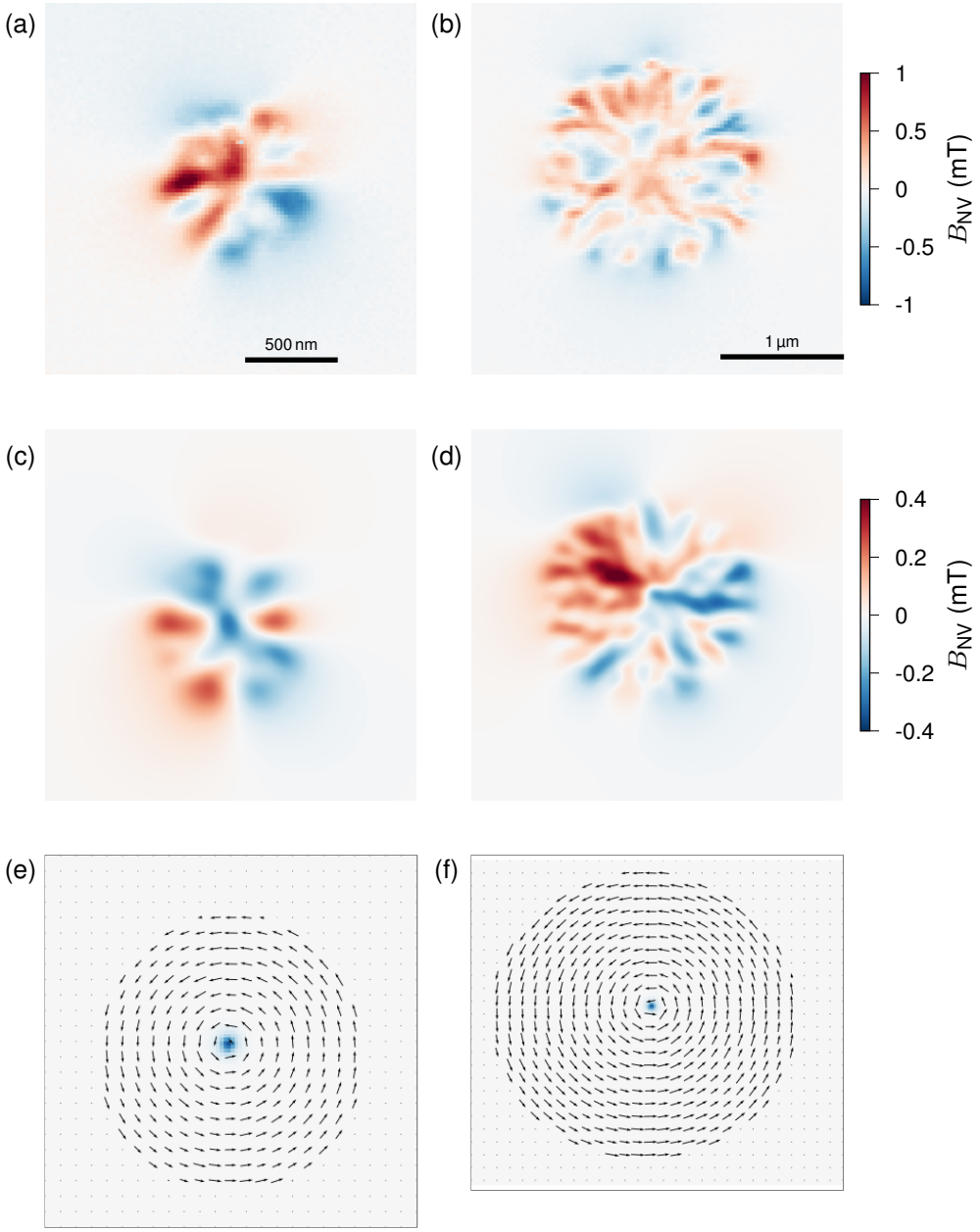

FIG. S5. (a)-(b) Measured stray field maps of vortices in discs microstructures. (c)-(d) Computed stray field maps resulting from the magnetic state shown in (e)-(f). (e)-(f) Magnetization configurations obtained from micromagnetic calculations with the parameters from Table I, with the blue color indicating the core of the vortices where the magnetization tilts out-of-plane. The field strength is significantly lower than in the measurement, probably because d_{NV} was actually smaller than 120 nm during this experiment.

VIII. MAGNETIZATION CONFIGURATIONS FOR VARIOUS SIZES OF MICROSTRUCTURES

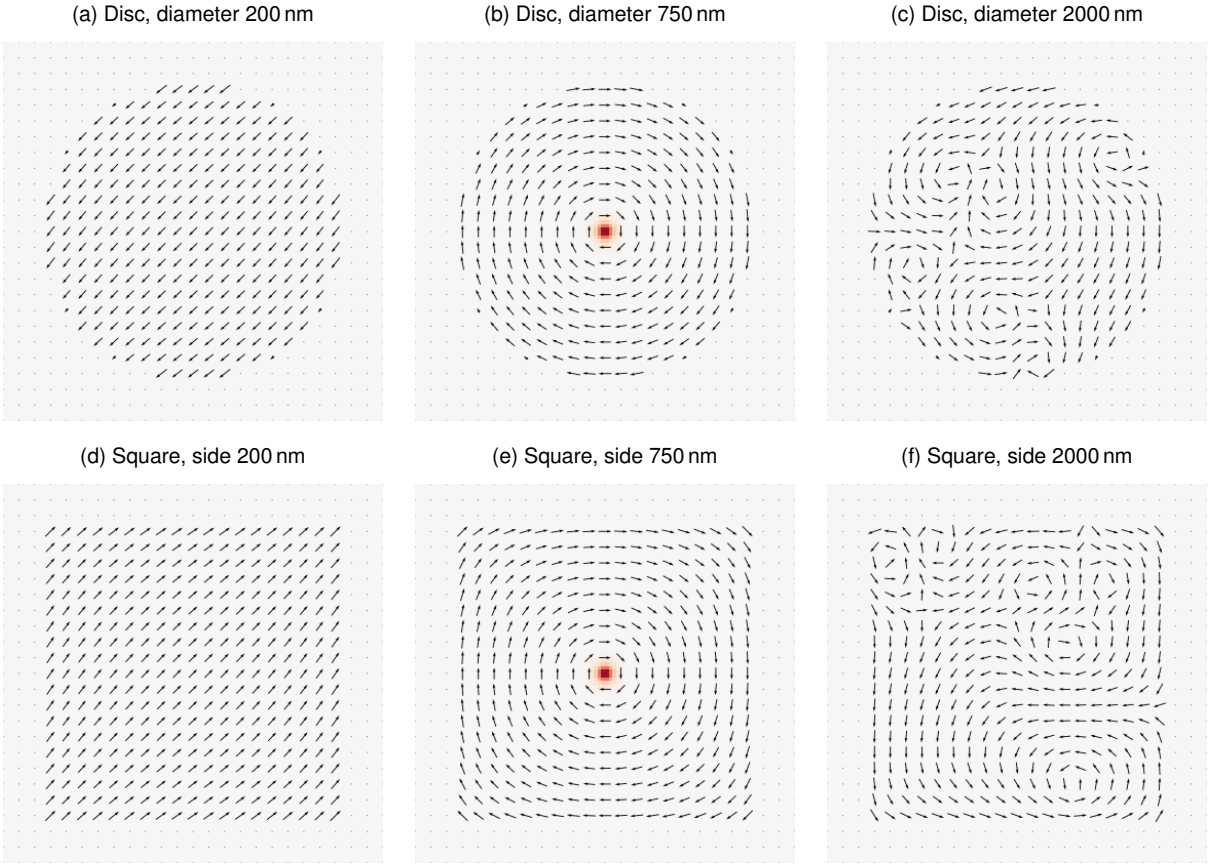

FIG. S6. Typical magnetization configurations obtained during the micromagnetic simulations presented in Fig. 4, starting from a random state. (a)-(c) Discs of increasing diameter, exhibiting respectively an uniform state, a single vortex and a multi vortices and antivortices state. The cores are not visible in the multivortices states because the simulated sample cells are too small. (d)-(f) Similar magnetization configurations obtained in squares.

IX. MAGNETIC TEXTURES AT 100 K

In order to determine the expected magnetic state of the microstructures at 100 K, we have performed micromagnetic simulations with the same parameters as in Fig. 2, but with $K_u = -129\,\mathrm{kJ\,m^{-3}}$ and $M_s = 575\,\mathrm{kA\,m^{-1}}$, as measured by SQUID on the reference sample [5]. Vortices are also stable, but their cores of are not resolved in the stray field maps (except for the ideal disc) because their diameter is very small (8 to 10 nm). Their stray field is therefore very weak (about 100 µT at 120 nm from the sample) and masked by the other field contributions.

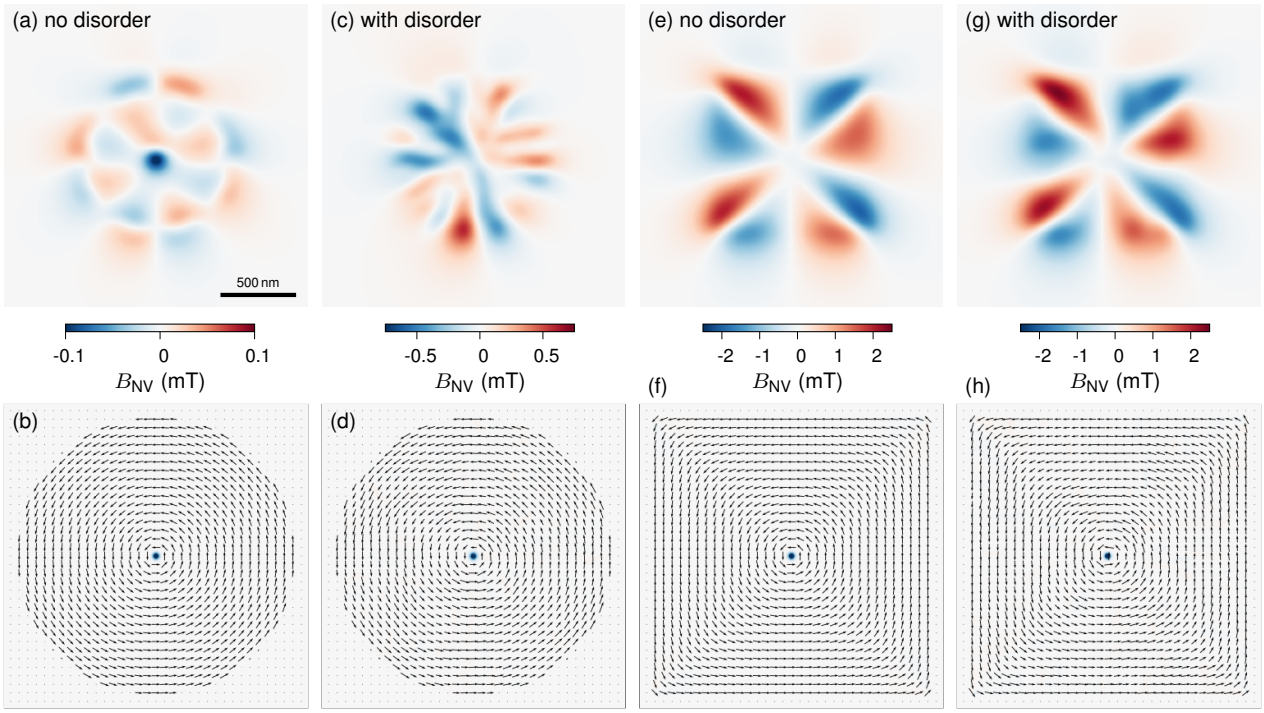

FIG. S7. Stray field maps (projected along the NV axis) computed from the magnetic states shown in the bottom row. The magnetic configurations are the results of micromagnetic simulations using the saturation magnetization and the uniaxial anisotropy measured at 100 K. The cores of the vortices are very small (8-10 nm), and are therefore not producing a strong enough field to be visible, except for the case of the perfect disc, for which the in-plane part of the vortex produces only a vanishingly small field.

[1] T. Hingant, J.-P. Tetienne, L. J. Martínez, K. Garcia, D. Ravelosona, J.-F. Roch, and V. Jacques, Measuring the Magnetic Moment Density in Patterned Ultrathin Ferromagnets with Submicrometer Resolution, Physical Review Applied **4**, 014003 (2015).

[2] I. Gross, W. Akhtar, V. Garcia, L. J. Martínez, S. Chouaieb, K. Garcia, C. Carrétéro, A. Barthélémy, P. Appel, P. Maletinsky, J.-V. Kim, J. Y. Chauleau, N. Jaouen, M. Viret, M. Bibes, S. Fusil, and V. Jacques, Real-space imaging of non-collinear antiferromagnetic order with a single-spin magnetometer, Nature **549**, 252 (2017).

[3] F. Fabre, A. Finco, A. Purbawati, A. Hadj-Azzem, N. Rougemaille, J. Coraux, I. Philip, and V. Jacques, Characterization of room-temperature in-plane magnetization in thin flakes of $CrTe_2$ with a single-spin magnetometer, Physical Review Materials **5**, 034008 (2021).

[4] Q. Li, M. Yang, C. Gong, R. V. Chopdekar, A. T. N'Diaye, J. Turner, G. Chen, A. Scholl, P. Shafer, E. Arenholz, A. K. Schmid, S. Wang, K. Liu, N. Gao, A. S. Admasu, S.-W. Cheong, C. Hwang, J. Li, F. Wang, X. Zhang, and Z. Qiu, Patterning-Induced Ferromagnetism of Fe_3GeTe_2 van der Waals Materials beyond Room Temperature, Nano Letters **18**, 5974 (2018).

[5] M. Ribeiro, G. Gentile, A. Marty, D. Dosenovic, H. Okuno, C. Vergnaud, J.-F. Jacquot, D. Jalabert, D. Longo, P. Ohresser, A. Hallal, M. Chshiev, O. Boulle, F. Bonell, and M. Jamet, Large-scale epitaxy of two-dimensional van der Waals room-temperature ferromagnet Fe_5GeTe_2, npj 2D Materials and Applications **6**, 1 (2022).